ORIGINAL PAPER

Comprehensive Analysis of Static, Buckling, and Free Vibration Behavior of Carbon Nanotube Reinforced Composite Plates on Pasternak's Elastic Foundation

Surya Dev Singh[1] · Rosalin Sahoo[2]

Abstract

Purpose This paper presents an in-depth analysis of the static, buckling, and free vibration behavior of carbon nanotube reinforced composite (CNTRC) plates resting on Pasternak's elastic foundation. The displacement field for the analysis is formulated using a secant function-based non-polynomial shear deformation theory, which captures the effects of transverse shear deformation more accurately than traditional polynomial-based theories. The governing differential equations are derived using Hamilton's principle and subsequently solved using Navier's solution method for CNTRC plates with simply supported boundary conditions. The novelties of this study include a comprehensive exploration of various parametric conditions, such as different volume fractions and distributions of carbon nanotubes, and variations in the foundation stiffness parameters (shear layer and Winkler modulus), providing deeper insights into the mechanical behavior of CNTRC plates under realistic loading conditions.

Methods The study incorporates various parametric conditions, including different volume fractions and distributions of carbon nanotubes, and variations in the foundation stiffness parameters (shear layer and Winkler modulus). The influence of these parameters on the mechanical behavior of CNTRC plates is systematically investigated.

Results Results demonstrate the significant impact of the Pasternak's foundation parameters and carbon nanotube reinforcement on the static deflection, critical buckling load, and natural frequencies of the plates. The analysis reveals that an appropriate selection of the foundation stiffness and nanotube distribution can significantly enhance the structural performance of CNTRC plates.

Conclusion This research provides valuable insights into the design and optimization of CNTRC plates on Pasternak's foundations, highlighting their potential applications in advanced engineering structures where enhanced mechanical properties and stability are crucial.

Keywords Carbon nanotube reinforced composite (CNTRC) · Pasternak elastic foundation · Secant function-based non-polynomial shear deformation theory · Hamilton's principle · Navier's solution method · Static, buckling, and free vibration analysis

Introduction

Since being first identified in 1991 by Iijima [6], carbon nanotubes (CNTs) have been in high demand in a variety of industries, including mechanical, biomechanics, chemical, aeronautical, electronics, and automobiles [1–5]. CNTs' outstanding chemical and mechanical properties have contributed to the sudden increase in demand. Since graphene sheet is the starting material for CNT production, their mechanical characteristics are comparable [7, 8]. When a single graphene sheet or more than one graphene sheet is rolled together into a concentric cylinder, the CNTs are referred to

✉ Rosalin Sahoo
  rosalin.civ@iitbhu.ac.in

1 Civil Engineering Department, Madanapalle Institute of Technology and Science, Madanapalle, Andhra Pradesh 517325, India

2 Civil Engineering Department, Indian Institute of Technology (Banaras Hindu University), Varanasi, UP 221005, India

Springer

as single walled carbon nano tubes (SWCNTs) [9, 10] and multi walled carbon nano tubes (MWCNTs) [11].

The mechanical behavior of composite plates, particularly those reinforced with carbon nanotubes (CNTs), has been a subject of extensive research due to the exceptional mechanical properties of CNTs. Previous studies have demonstrated the significant improvements in stiffness, strength, and thermal properties that CNT reinforcement can bring to composite materials. The incorporation of CNTs into polymer matrices has been shown to enhance the overall performance of composite plates, making them suitable for advanced engineering applications [1–5]. Since their discovery by Iijima [6] in 1991, carbon nanotubes (CNTs) have been extensively studied for their exceptional mechanical properties, which are akin to those of graphene, the precursor material for CNT production [7, 8]. CNTs are categorized based on their structure: single-walled carbon nanotubes (SWCNTs) [9, 10], formed by rolling a single graphene sheet into a cylinder, and multi-walled carbon nanotubes (MWCNTs) [11], created by rolling multiple graphene sheets into concentric cylinders. The analysis of composite plates on elastic foundations has garnered significant attention due to the critical role of the interaction between the plate and the foundation in determining structural behavior under various loading conditions. Pasternak's elastic foundation model, which incorporates both shear layer and Winkler modulus parameters, provides a more accurate representation of this interaction compared to the simpler Winkler model (Pasternak, 1954). Recent review articles have synthesized current developments in CNT research, addressing factors such as development, numerical implementation, structural advancement, and applications [12–15]. Ajayan et al. [16] introduced the initial structural application of CNTs as reinforcement with polymers, leading to their acceptance in elastic structures [17–19]. Wattanasakulpong and Ungbhakorn [20] employed several shear deformable theories to provide an analytical solution for the bending analysis of CNTRC beams with Winkler-Pasternak elastic foundations. Their research demonstrated that a functionally graded (FG)-X reinforcement distribution of CNTs effectively counteracts bending responses. Yas and Samadi [21] used Timoshenko beam theory to investigate the free vibration of CNTRC beams, finding that FG-X distribution yields the highest natural frequency. Shen and Xiang [22] used high order shear deformation theory (HSDT) to examine the non-linear bending behavior of CNTRC beams on Winkler elastic foundations. They investigated various CNT distribution patterns, finding that FG-A CNTs generate the highest transverse deflection. They also studied the non-linear bending behavior of CNTRC shells on Pasternak elastic foundations, revealing the impact of volume fraction and foundation parameters on non-linear bending behavior [23]. Additionally, they explored the effect of temperature rise on the

natural frequency of CNTRC shells, showing that increased temperature leads to a decrease in natural frequency [24]. Zhang et al. [25] applied element-free IMLS-Ritz methods for non-linear buckling analysis of CNTRC plates on Winkler foundations and conducted non-linear bending analysis for similar systems [26]. Wattanasakulpong and Chaikittiratana [27] used third-order shear deformation theory (TSDT) and sinusoidal shear deformation theory (SSDT) to analyze static and dynamic responses of CNTRC plates with Pasternak elastic foundations, highlighting the effectiveness of FG-X reinforcement in balancing bending responses. Lei et al. [28] employed first-order shear deformation theory (FSDT) to analyze the buckling of CNTRC plates with Pasternak elastic foundations, concluding that volume fraction and foundation parameters significantly influence critical buckling loads. Their vibration analysis further confirmed the impact of these parameters on natural frequency [29]. Zhang and Liew [30] investigated the non-linear bending behavior of CNTRC skew plates on elastic foundations using FSDT, demonstrating the influence of skew angle and foundation parameters. Further studies explored various aspects of CNTRC structures on elastic foundations. Keleshteri et al. [31] analyzed vibration behavior of angular CNTRC plates with piezoelectric layers. Kutlu and Omurtag [32] examined bending behavior of elliptical CNTRC plates, and Duc et al. [33] investigated buckling of angular conical shells on elastic foundations. Ansari et al. [34] utilized the variational differential quadrature method to study free vibration of functionally graded carbon nanotube-reinforced composite (FG-CNTRC) structures. Tham et al. [35] introduced a refined shell theory for analyzing free vibration behavior of multi-layered FG-CNTRC shallow shell panels. Thi et al. [36] applied the cell-based smoothed discrete shear gap method for static and free vibration analysis of CNTRC plates. Zghal et al. [37] explored free vibration in functionally graded composite shell structures reinforced by CNTs. Forooghi et al. [38] investigated stability and vibration properties of FG-SWCNTRC plates using higher-order shear deformation theory and a Visco-Hetenyi medium. Thai et al. [39] developed a size-dependent meshfree model for FG CNTRC nanoplates, integrating higher-order shear deformation plate theory with nonlocal Eringen elasticity theory. They also proposed a NURBS formulation based on refined plate theory for comprehensive analysis of multilayer FG GPLRC plates [40]. Daikh et al. [41] examined thickness stretching effects on multilayer FG CNTRC nanoplates, enhancing understanding of their free vibration, stability, and bending characteristics. Sharma et al. [42] studied buckling and free vibration traits of FG CNT-reinforced plates using an inverse hyperbolic shear deformation theory. Uymaz and Uymaz [43] explored three-dimensional thermal vibration analysis of FG-CNT reinforced composite plates under varying temperature distributions. Li et al. [44]

investigated the nonlinear thermally induced vibration in sandwich beams with auxetic honeycomb cores under varied boundary conditions. Using first-order shear deformation theory and considering geometric nonlinearity and temperature effects, it employs finite element analysis and Newton–Raphson–Newmark method. Findings highlight how altering honeycomb geometry and thermal conditions can mitigate vibration, aiding in beam design. Zhang et al. [45] studied the graphene platelet (GPL)-reinforced nanocomposite lattice sandwich plates under supersonic airflow, integrating temperature- and moisture-dependent properties. It assesses GPL distribution and reinforcement in truss cores, employing Halpin–Tsai model for elasticity, and rule of mixture for properties. Flutter analysis via Lagrange method considers aerodynamic loads, emphasizing impacts of temperature, moisture, and GPL parameters on aero-thermoelastic behavior. Wang et al. [46] employed a nonlinear energy sink (NES) to mitigate nonlinear aeroelastic responses in graphene platelet reinforced composite (GPLRC) lattice sandwich plates under supersonic airflow. It integrates Halpin–Tsai model for material properties, Kirchhoff and shear deformation theories for structural modeling, and Newmark method for analysis, showing effective suppression of flutter behavior with NES intervention. Yang et al. [47] examined the nonlinear free vibration and bifurcation in a carbon fiber-reinforced plastic (CFRP) truncated laminated conical shell using first-order shear deformation theory. It formulates governing equations via Hamilton's principle and Galerkin method, analyzing temperature and shell geometry effects on vibration behavior through parametric investigation. Yang et al. [48] investigated the static bending and buckling behavior of a simply supported truncated sandwich conical shell with a variable thickness core. The core's porous structure varies along its length, influencing system stiffness. Utilizing Hamilton's principle, First-Order Shear Deformation Theory (FSDT), and the Galerkin method, matrix equations are derived to analyze deflections and critical buckling loads under thermal conditions. Static properties and modes of the system are thoroughlyexamined, considering five different porosity distribution schemes for the foam core. Wang et al. [49] carried out the modelling and analysis for the free vibration of a truncated sandwich conical shell with a variable stiffness system, using a porous aluminum foam core and carbon fiber face sheets under simply supported conditions. It considers various porosity distributions and thermal effects, deriving nonlinear dynamic equations with first-order shear deformation theory and Hamilton's principle. The study comprehensively examines natural frequencies, mode shapes, and their dependencies on key parameters. Yang et al. [50] investigated the static and dynamic stability of a laminated CFRP cylindrical shell under a non-normal boundary condition. It applies Hamilton's principle and von-Karman relationships with first-order

shell theory, deriving equations via the Galerkin method. Stability is analyzed using eigenvalue analysis and the Bolotin method, exploring key influences on stability. Yang et al. [51] investigated the nonlinear dynamic responses and bifurcations of a truncated sandwich conical shell with varying thickness and porous core under 1:1 internal resonance. Using FSDT, von-Karman theory, Hamilton's principle, and Galerkin method, it explores dynamic formulations, resonance effects, and influences of damping, detuning, temperature, and excitations. Chai et al. [52] carried out the free vibration of variable thickness graphene-reinforced porous cylindrical curved plates under simply supported boundaries. It employs the Halpin–Tsai model, mixing rule, FSDT, and Hamilton's principle to derive nonlinear dynamic equations and determine natural frequencies. Factors influencing frequencies and modal shapes are comprehensively analyzed. Grover et al. [53] proposed a shear deformation theory based on a secant function (SDTSF) for predicting static and dynamic characteristics of laminated composite plates. This theory does not require a shear correction factor as it satisfies the traction-free boundary conditions at the plate's top and bottom surfaces. The investigations confirmed SDTSF's effectiveness in predicting both static and dynamic behavior of laminated composite plates.

It is identified from the literature investigation that a lack of an analytical model for the bending, buckling and free vibration responses of the CNTRC plate resting on the Pasternak's elastic foundation with shear layer and Winkler springs in the framework of non-polynomial shear deformation theory based on secant function. In the current study, An analytical model for the bending, buckling, and free vibration responses of the CNTRC plate resting on the Pasternak's elastic foundation has been provided in order to fill in the informed gap in the literature. The bending, buckling, and free vibration behaviours of the CNTRC plate are examined under a variety of parametric conditions, including different CNTs volume fractions, CNTs distribution patterns, side thickness ratios, and spring constant factors. The bending, free vibration, and buckling of plates are carefully investigated and addressed in this study.

In conclusion, this research advances the understanding of CNTRC plate mechanics on Pasternak's foundations by elucidating the intricate interplay between material composition and foundation characteristics. The findings underscore the potential for tailored designs that optimize structural performance through judicious selection of foundation stiffness and carbon nanotube distribution. Such insights are critical for the development of robust CNTRC-based engineering structures that exhibit enhanced mechanical properties and stability, thereby opening new avenues for their application in demanding technological fields.
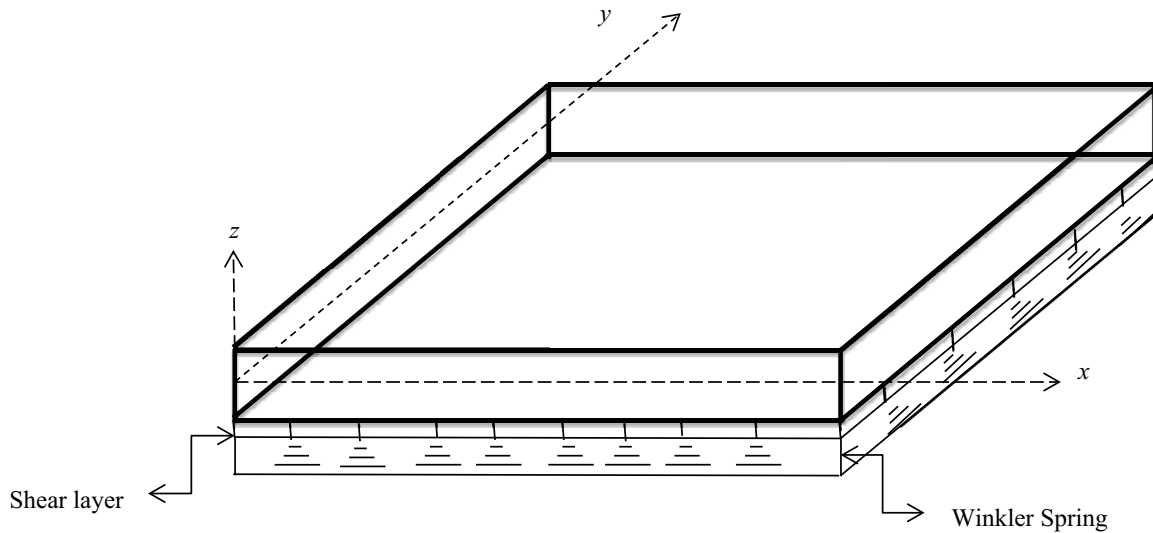
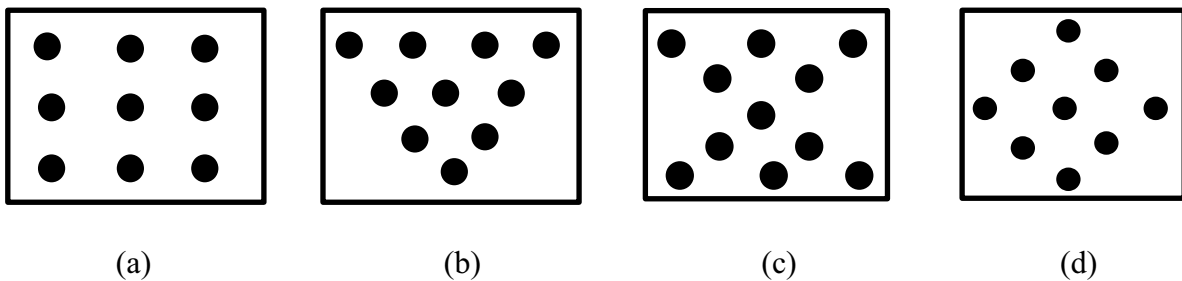**Fig. 1** CNTRC plate resting on the Pasternak's elastic foundation

Fig. 2 Cross section of CNTRC plate with different distribution pattern of CNTs **a** UD **b** FG-V **c** FG-X **d** FG-O

Geometrical Models and Properties

Figure 1 represents the CNTRC plate resting on the Pasternak elastic foundation with the Winkler spring and shear layer. The selected CNTRC plate includes the following dimensions: (a), (b), and (h) as length, width, and height respectively. Here, multiple dispersions of CNTs patterns that have been uniaxially aligned across the thickness of the CNTRC plate are taken into consideration for the study. For UD, FG-X, and FG-O reinforced CNTRC plates, the CNTs distribution patterns are symmetrical; for FG-V reinforced CNTRC plates, they are asymmetrical. Figure 2 displays the cross sections of the CNTRC plate with various CNTs dispersion patterns.

Due to the different categories CNTs dispersion patterns throughout the plate's thickness, the mechanical properties of CNTRC plates change along with thickness. Table 1 lists the mathematical relationships that describe the different types of reinforcing distribution throughout

Table 1 Distribution relationship of CNTRC plates

Distribution FG	Distribution relationship
UD CNTRC plate	$V_{CNT} = V_{CNT}^*$
FG-V CNTRC plate	$V_{CNT} = \left(1 + \frac{2z}{h}\right)V_{CNT}^*$
FG-O CNTRC plate	$V_{CNT} = 2\left(1 - \frac{2|z|}{h}\right)V_{CNT}^*$
FG-X CNTRC plate	$V_{CNT} = 2\left(\frac{2|z|}{h}\right)V_{CNT}^*$

the thickness of the composite plates. Table 2 lists the mechanical properties of the different elements of the CNTRC plate, specifically SWCNTs as reinforcement fibre and PmPV (methyl methacrylate-co-polyvinyl acetate) as the polymer matrix. The volume fraction of the CNTs influences the effectiveness of CNTRC plate. In Table 3, the efficiency parameter, η_i, for various CNTs volume fractions are listed.

Table 2 Material properties used for CNTRC plates

Material	E_1 (GPa)	$E_2 = E_3$ (GPa)	$G_{12} = G_{12} = G_{12}$ (GPa)	$\upsilon_{12} = \upsilon_{23} = \upsilon_{13}$	ρ (kg/m^3)
CNTs	5646.6	7080	1944.5	0.175	1400
PmPV(M1)	2.1	2.1	0.7835	0.34	1150

Table 3 CNTs efficiency parameter for PmPV (M2)/CNT

V_{CNT}^*	η_1	η_2	η_3
0.11	0.149	0.934	0.934
0.14	0.150	0.941	0.941
0.17	0.149	1.381	1.381

Rule of mixture (ROM) has been employed for analysing the mechanical properties of CNTRC plate and it is described as follows:

$$E_{11} = (\eta_1)V_{CNT}E_{11}^{CNT} + V_m E^m \tag{1a}$$

$$\frac{(\eta_2)}{E_{22}} = \frac{V_{CNT}}{E_{22}^{CNT}} + \frac{V_m}{E^m} \tag{1b}$$

$$\frac{(\eta_3)}{G_{12}} = \frac{V_{CNT}}{G_{22}^{CNT}} + \frac{V_m}{G^m} \tag{1c}$$

$$v_{12} = V_{CNT}^* v_{12}^{CNT} + V_m v^m \tag{1d}$$

$$\rho = V_{CNT}\rho^{CNT} + V_m \rho^m \tag{1e}$$

where, E_{11}, E_{11}^{CNT}, E^m, E_{22} and E_{22}^{CNT} are the Young's moduli. G_{12}, G_{12}^{CNT} and G^m are the shear modulus. v_{12}, v_{12}^{CNT} and v^m are the Poisson's ratios. V_{CNT}^* and V_m are the volume fraction of CNTs and isotropic matrix. η_i (i = 1–3) is the coefficients of the CNTs efficiency parameters.

$$V_{CNT}^* + V_m = 1 \tag{2}$$

where, V_{CNT}^* is expressed as,

$$V_{CNT}^* = \frac{w_{CNT}}{w_{CNT} + (\rho^{CNT}/\rho^m) - (\rho^{CNT}/\rho^m)w_{CNT}} \tag{3}$$

where w_{CNT} is the mass fraction of the CNTs.

Mathematical Formulations

Displacement Field

The displacement field for non-polynomial shear deformation theory based on secant function [44] is chosen in order to forecast both the static and dynamic behaviour of the CNTRC plate supported by the Pasternak's elastic foundation. The non-polynomial trigonometric function is selected here in such a way that it generates a non-linear distribution of transverse shear stresses. The transverse shear stress boundary conditions are implemented so that the transverse shear stresses at the boundary vanish, and this allows us to assess a constant parameter. Thus, the shear correction factor is no longer necessary because the considered non-polynomial displacement field fulfils the traction-free boundary conditions at the top and bottom of the plate.

$$\begin{bmatrix} u(x,y,z,t) \\ v(x,y,z,t) \\ w(x,y,z,t) \end{bmatrix} = \begin{bmatrix} u_0(x,y,t) \\ v_0(x,y,t) \\ w_0(x,y,t) \end{bmatrix} - z\begin{bmatrix} \frac{\partial w_0(x,y,t)}{\partial x} \\ \frac{\partial w_0(x,y,t)}{\partial y} \\ 0 \end{bmatrix} + f(z)\begin{bmatrix} \theta_x(x,y,t) \\ \theta_y(x,y,t) \\ 0 \end{bmatrix} \tag{4}$$

where u_0, v_0, w_0, and θ_x, θ_y are the displacement and shear deformations at the mid plane, respectively. $f(z) = g(z) + \Omega z$ in which $g(z) = z(\sec(rz/h))$ and $\Omega = -\sec(r/2) [1 + (r/2) \tan(r/2)]$. The value of the transvers shear stress parameter i.e. $r = 0.1$.

The strain in conjunction with the displacement field is expressed as follows:

$$\begin{bmatrix} \varepsilon_{xx} \\ \varepsilon_{yy} \\ \gamma_{xy} \end{bmatrix} = \begin{bmatrix} \frac{\partial u_0}{\partial x} \\ \frac{\partial v_0}{\partial y} \\ \left(\frac{\partial u_0}{\partial y} + \frac{\partial v_0}{\partial x}\right) \end{bmatrix} - z\begin{bmatrix} \frac{\partial^2 w_0}{\partial x^2} \\ \frac{\partial^2 w_0}{\partial y^2} \\ \frac{2\partial^2 w_0}{\partial x \partial y} \end{bmatrix} + [g(z) + \Omega z]\begin{bmatrix} \frac{\partial \theta_x}{\partial x} \\ \frac{\partial \theta_y}{\partial y} \\ \left(\frac{\partial \theta_x}{\partial y} + \frac{\partial \theta_y}{\partial x}\right) \end{bmatrix} \tag{5a}$$

$$\begin{bmatrix} \gamma_{xz} \\ \gamma_{yz} \end{bmatrix} = f'(z)\begin{bmatrix} \theta_x \\ \theta_y \end{bmatrix} \tag{5b}$$

The stress in conjunction with the strain is expressed as follows:

$$\begin{bmatrix} \sigma_{xx} \\ \sigma_{yy} \\ \tau_{xy} \\ \tau_{yz} \\ \tau_{xz} \end{bmatrix}_n = \begin{bmatrix} Q_{11} & Q_{12} & Q_{16} & 0 & 0 \\ Q_{21} & Q_{22} & Q_{26} & 0 & 0 \\ Q_{16} & Q_{26} & Q_{66} & 0 & 0 \\ 0 & 0 & 0 & Q_{44} & Q_{45} \\ 0 & 0 & 0 & Q_{45} & Q_{55} \end{bmatrix}_n \begin{bmatrix} \varepsilon_{xx} \\ \varepsilon_{yy} \\ \gamma_{xy} \\ \gamma_{yz} \\ \gamma_{xz} \end{bmatrix}_n \tag{6}$$

where, $[Q]_n$ is known as the reduced stiffness matrix and it is used to relate the stress and strain vectors of the nth layer. The elements of reduced stiffness matrix are the functions of material properties E_{11}, E_{22}, G_{12}, G_{23}, G_{13}, and ν_{12} which

are function of thickness co-ordinate and depend upon the distribution of CNTs across the thickness. These elements are defined as

$$Q_{11}(z) = \frac{E_{11}(z)}{1 - v_{12}(z)v_{21}(z)}, \; Q_{22}(z) = \frac{E_{22}(z)}{1 - v_{12}(z)v_{21}(z)},$$

$$Q_{12}(z) = \frac{v_{21}(z)E_{11}(z)}{1 - v_{12}(z)v_{21}(z)}, \; Q_{66}(z) = G_{12}(z) \, Q_{44}(z)$$

$$= G_{23}(z), \; Q_{55}(z) = G_{13}(z)$$

Equation of Motion

The equation of motion of the CNTRC plate with Pasternak's elastic basis is derived using Hamilton's principle.

$$\int_{-h/2}^{h/2} (\delta L)dt = 0 \tag{7}$$

where $\delta L = \delta T - (\delta U_s + \delta V_f + \delta V)$; δT, δU_s, δV_f, and δV are the change in kinetic energy, change in strain energy, change in potential energy of elastic foundation and change in potential energy due to external applied load, respectively.

The change in the kinetic energy of the system is expressed as follows:

$$\delta T = \int_{\Omega_0} \left\{ \int_{-\frac{h}{2}}^{\frac{h}{2}} \rho[\dot{u}\delta\dot{u} + \dot{v}\delta\dot{v} + \dot{w}\delta\dot{w}]dz \right\}dxdy \tag{8}$$

The change in the strain energy of the system is expressed as follows:

$$\delta U = \int_{\Omega_0} \left\{ \int_{-\frac{h}{2}}^{\frac{h}{2}} [\sigma_{xx}\delta \in_{xx} + \sigma_{yy}\delta \in_{yy} + \tau_{xy}\delta\gamma_{xy} + \tau_{yz}\delta\gamma_{yz} + \tau_{zx}\delta\gamma_{zx}]dz \right\}dxdy \tag{9}$$

where, $\delta \in$ is the small variation in the strain at any point in the nth lamina defined in the material coordinate's axes system.

The change in the potential energy of the system due to external applied load is expressed as follows:

$$\delta V = \int_{\Omega_0} q\delta w_0 dxdy \tag{10}$$

The change in the potential energy of the system due to Pasternak elastic foundation is expressed as follows:

$$\delta V_f = \int_{\Omega_0} k_w w_0\delta w_0 dxdy + \int_{\Omega_0} k_s(\frac{\partial w_0}{\partial x}\frac{\partial\delta w_0}{\partial x} + \frac{\partial w_0}{\partial y}\frac{\partial\delta w_0}{\partial y})dxdy \tag{11}$$

where K_w and K_s are the Winkler and shear layer spring constants, respectively

$$K_w = \frac{\beta_w D_0}{a^4}$$

$$K_s = \frac{\beta_s D_0}{a^2}$$

$$D_0 = \frac{E^p h^3}{12[1 - (v^p)^2]}$$

here, β_w and β_s are the Winkler and shear layer spring constant factor, respectively.

The CNTRC plate with Pasternak elastic foundation is subjected to the transverse load q, which is the bending load and the in-plane compressive load of $\Psi_x N_{cr}$ and $\Psi_y N_{cr}$ which is the buckling load in x and y direction, respectively. The total potential energy of the system due to external applied load is expressed as follows:

$$\delta V_T = -\int_{\Omega_0} q\delta w_0 dxdy$$
$$+ \int_{\Omega_0} (\psi_x N_{cr}\frac{\partial w_0}{\partial x}\frac{\partial\delta w_0}{\partial x} + \psi_y N_{cr}\frac{\partial w_0}{\partial y}\frac{\partial\delta w_0}{\partial y})dxdy \tag{12}$$

The mid-plane displacement and rotation coefficients are separated, and the variation of the system's energies from Eqs. (8) to (12) is substituted in Eq. (7), Partial differential equation terms of the primary variables are separated for different displacement modes derived at the mid plane are shown in Appendix A. This process results in the development of the governing differential equation for the CNTRC plate with Pasternak's elastic foundation, which is as follows:

$$\delta u_0 : \frac{\partial N_{xx}}{\partial x} + \frac{\partial N_{xy}}{\partial y} = I_0\ddot{u}_0 - I_1\frac{\partial\ddot{w}_0}{\partial x} + I_3\ddot{\theta}_x \tag{13a}$$

$$\delta v_0 : \frac{\partial N_{xy}}{\partial x} + \frac{\partial N_{yy}}{\partial y} = I_0\ddot{v}_0 - I_1\frac{\partial\ddot{w}_0}{\partial y} + I_3\ddot{\theta}_y \tag{13b}$$

$$\delta w_0 : \frac{\partial^2 M_{xx}}{\partial x^2} + 2\frac{\partial^2 M_{xy}}{\partial x\partial y} + \frac{\partial^2 M_{yy}}{\partial y^2} + q - k_w w_0 + k_s\frac{\partial^2 w_0}{\partial x^2}$$
$$+ k_s\frac{\partial^2 w_0}{\partial y^2} + \overline{N}_{xx}\frac{\partial^2 w_0}{\partial x^2} + 2\overline{N}_{xy}\frac{\partial^2 w_0}{\partial x\partial y} + \overline{N}_{yy}\frac{\partial^2 w_0}{\partial y^2}$$
$$= I_1\left(\frac{\partial\ddot{u}_0}{\partial x} + \frac{\partial\ddot{v}_0}{\partial y}\right) - I_2\left(\frac{\partial^2\ddot{w}_0}{\partial x^2} + \frac{\partial^2\ddot{w}_0}{\partial y^2}\right) + I_4\left(\frac{\partial\ddot{\theta}_x}{\partial x} + \frac{\partial\ddot{\theta}_y}{\partial y}\right) + I_0\ddot{w}_0 \tag{13c}$$

$$\delta\theta_x : \Omega\frac{\partial M_{xx}}{\partial x} + \frac{\partial P_{xx}}{\partial x} + \Omega\frac{\partial M_{xy}}{\partial y} + \frac{\partial P_{xy}}{\partial y}$$
$$- \Omega Q_1 - K_1 = I_3\ddot{u}_0 - I_4\frac{\partial\ddot{w}_0}{\partial y} + I_5\ddot{\theta}_x \tag{13d}$$

$$\delta\theta_y : \Omega \frac{\partial M_{xy}}{\partial x} + \frac{\partial P_{xy}}{\partial x} + \Omega \frac{\partial M_{yy}}{\partial y} + \frac{\partial P_{yy}}{\partial y}$$

$$- \Omega Q_2 - K_2 = I_3 \ddot{v}_0 - I_4 \frac{\partial \ddot{w}_0}{\partial y} + I_5 \ddot{\theta}_y \tag{13e}$$

The moment resultants associated with the governing differential equation of the CNTRC plate with Pasternak elastic foundation Eq. (13) is as follows:

$$\begin{bmatrix} N_{xx} & M_{xx} & P_{xx} \\ N_{yy} & M_{yy} & P_{yy} \\ N_{xy} & M_{xy} & P_{xy} \end{bmatrix} = \int_{h_k}^{h_{k+1}} \begin{Bmatrix} \sigma_{xx} \\ \sigma_{yy} \\ \tau_{xy} \end{Bmatrix} [1 \ z \ g(z)] \, dz \tag{14}$$

$$\begin{bmatrix} Q_2 & K_2 \\ Q_1 & K_1 \end{bmatrix} = \int_{h_k}^{h_{k+1}} \begin{Bmatrix} \tau_{yz} \\ \tau_{xz} \end{Bmatrix} [1 \ g'(z)] \, dz \tag{15}$$

$$[I_0 \ I_1 \ I_2 \ I_3 \ I_4 \ I_5] = \int_{h_k}^{h_{k+1}} \rho^{(k)} [1 \ z \ z^2 \ f(z) \ z.f(z) \ (f(z))^2] \, dz \tag{16}$$

$$[A_{ij} \ B_{ij} \ D_{ij} \ E_{ij} \ F_{ij} \ H_{ij}] = \int_{h_k}^{h_{k+1}} \left[\overline{Q}_{ij}^{(k)}\right] [1 \ z \ z^2 \ g(z) \ z.g(z) \ (g(z))^2] \, dz \tag{17}$$

for $i, j = 1, 2$, and 3.

$$[K_{ij} \ L_{ij}] = \int_{h_k}^{h_{k+1}} \left[\overline{Q}_{ij}^{(k)}\right]_{2\times2} [g'(z) \ (g'(z))^2] \, dz \tag{18}$$

for $i, j = 4$ and 5.

Analytical Solution Methodology

Using Navier's method, the governing differential equation of the CNTRC plate with the Pasternak elastic foundation Eq. (13) is solved. The CNTRC plate is simply supported from all four sides using the following boundary requirements.

at $y = 0, y = b$(parallel to x axis)
$u_0 = 0, w_0 = 0, \theta_x = 0, N_{yy} = 0, M_{yy} = 0, P_{yy} = 0.$
at $x = 0, x = l$(parallel to y axis)
$v_0 = 0, w_0 = 0, \theta_y = 0, N_{xx} = 0, M_{xx} = 0, P_{xx} = 0.$ \tag{19}

The displacement variables are assumed in such a way that it satisfies the above mentioned boundary condition requirements.

$$u_0 = \sum_{m=1}^{\infty} \sum_{n=1}^{\infty} u_{0_{mn}} e^{i\omega t} \cos(\alpha x) \sin(\beta y) \tag{20a}$$

$$v_0 = \sum_{m=1}^{\infty} \sum_{n=1}^{\infty} v_{0_{mn}} e^{i\omega t} \sin(\alpha x) \cos(\beta y) \tag{20b}$$

$$w_0 = \sum_{m=1}^{\infty} \sum_{n=1}^{\infty} w_{0_{mn}} e^{i\omega t} \sin(\alpha x) \sin(\beta y) \tag{20c}$$

$$\theta_x = \sum_{m=1}^{\infty} \sum_{n=1}^{\infty} \theta_{x_{mn}} e^{i\omega t} \cos(\alpha x) \sin(\beta y) \tag{20d}$$

$$\theta_y = \sum_{m=1}^{\infty} \sum_{n=1}^{\infty} \theta_{y_{mn}} e^{i\omega t} \sin(\alpha x) \cos(\beta y) \tag{20e}$$

where, $u_{0_{mn}}, v_{0_{mn}}, w_{0_{mn}}, \theta_{x_{mn}}$ and $\theta_{y_{mn}}$ are the arbitrary parameter, ω is the natural frequency $\alpha = m\pi/a$, and $\beta = m\pi/b$.

The transverse load q is defined as follow:

$$q_0 = \sum_{m=1}^{\infty} \sum_{n=1}^{\infty} q \sin(\alpha x) \cos(\beta y) \tag{21}$$

The simultaneous equation for static and dynamic analysis is obtained by substituting the assumed displacement variables from Eq. (20) into the governing differential equations of CNTRC plate resting on Pasternak's elastic foundation Eq. (13) that governs the CNTRC plate. This equation is as follows:

$$\left\{[K]_{5\times5} - \omega^2[M]_{5\times5}\right\} \begin{Bmatrix} u_0 \\ v_0 \\ w_0 \\ \theta_x \\ \theta_y \end{Bmatrix}_{5\times1} = \begin{Bmatrix} 0 \\ 0 \\ q \\ 0 \\ 0 \end{Bmatrix}_{5\times1} \tag{22}$$

where, $[K]$ and $[M]$ are the stiffness and mass matrix respectively, and the coefficients of mass matrix is discussed in Appendix B.

The in-plane compressive lode and natural frequency are removed from Eq. (22) for the static analysis of the CNTRC plate with Pasternak's elastic foundation, and Eq. (22) is then transformed into the simultaneous equation for the static analysis of the CNTRC plate with Pasternak elastic foundation. The determent of the coefficient of the load vector is equal to zero to produce the set of homogeneous equations for the buckling and free vibration analysis of the CNTRC plate with Pasternak's elastic basis. As an Eigen-value problem, the derived homogeneous equations are resolved.

Simultaneous Equations for Static and Dynamic Analysis

The simultaneous equation for static analysis of the CNTRC plate with Pasternak elastic foundation is mentioned as follows:

$$[K]_{5\times5}\begin{Bmatrix} u_0 \\ v_0 \\ w_0 \\ \theta_x \\ \theta_y \end{Bmatrix}_{5\times1} = \begin{Bmatrix} 0 \\ 0 \\ q \\ 0 \\ 0 \end{Bmatrix}_{5\times1} \tag{23}$$

The simultaneous equation for the buckling analysis of the CNTRC plate with Pasternak elastic foundation is mentioned as follows:

$$\left\{ [K]_{5\times5} - N_{cr}[G]_{5\times5} \right\}\begin{Bmatrix} u_0 \\ v_0 \\ w_0 \\ \theta_x \\ \theta_y \end{Bmatrix}_{5\times1} = \begin{Bmatrix} 0 \\ 0 \\ 0 \\ 0 \\ 0 \end{Bmatrix}_{5\times1} \tag{24}$$

where, N_{cr} and $[G]$ are the buckling load, and geometric stiffness matrix, respectively.

The governing equation for the vibration analysis of the CNTRC plate with Pasternak elastic foundation is mentioned as follows:

$$\left\{ [K]_{5\times5} - \omega^2[M]_{5\times5} \right\}\begin{Bmatrix} u_0 \\ v_0 \\ w_0 \\ \theta_x \\ \theta_y \end{Bmatrix}_{5\times1} = \begin{Bmatrix} 0 \\ 0 \\ 0 \\ 0 \\ 0 \end{Bmatrix}_{5\times1} \tag{25}$$

Results and Discussions

The findings of the banding, buckling and free vibration analysis of the CNTRC plate with the Pasternak's elastic foundation are carried out in detail in this part. The following non-dimensional parameter is used to provide the findings in dimensionless form.

$$\overline{w} = \frac{10^3 D_0 w}{a^4 q_0}\left(\frac{a}{2}, \frac{b}{2}, \frac{h}{2}\right) \tag{26}$$

$$\overline{\sigma}_{xx} = \sigma_{xx}\frac{h^2}{a^2 q_0}\left(\frac{a}{2}, \frac{b}{2}, \frac{h}{2}\right) \tag{27}$$

$$\overline{\tau}_{xz} = \tau_{xz}\frac{h^2}{a^2 q_0}\left(\frac{a}{2}, 0, 0\right) \tag{28}$$

$$\overline{\tau}_{xy} = \tau_{xy}\frac{h^2}{a^2 q_0}\left(a, b, \frac{h}{2}\right) \tag{29}$$

$$\overline{\omega} = \omega\frac{a^2}{h}\sqrt{\frac{\rho^m}{E^m}} \tag{30}$$

$$D_0 = \frac{E^p h^3}{12[1-(\nu^p)^2]}; \quad \overline{N}_{cr} = N_{cr}\frac{a^2}{\pi^2 D_0} \tag{31}$$

Static Analysis

This section goes into extensive detail on the static analysis of the CNTRC plate resting on Pasternak's elastic base.

Table 4 investigates the non-dimensional transverse displacement for the variations in CNTs distributions, considering different thickness ratios, CNT volume fractions, and spring constant factors. The FG-V, FG-O, and FG-X distributions, along with the UD distribution, are specifically analyzed in the context of CNTRC plates with and without a Pasternak's elastic foundation. These plates are composed of CNT fibers within a poly (methyl methacrylate)-polyvinylidene fluoride (PmPV) matrix. The analysis focuses on a square CNTRC plate with simple supported boundary conditions under sinusoidal loading. The findings are presented using a non-dimensional parameter as defined by Eq. (26). The non-dimensional transverse displacement data from this study are compared with those reported by Wattanasakulpong and Chaikittiratana [27]. For a side-to-thickness ratio of 10, the results align closely with those of Wattanasakulpong and Chaikittiratana [27]. It is apparent that among the reinforcement distributions examined UD, FG-O, FG-V, and FG-X, the FG-X distribution exhibits superior performance in minimizing non-dimensional transverse displacement, effectively countering bending responses in both the presence and absence of a Pasternak's elastic foundation. This superior performance can be attributed to the optimal gradation of CNTs in the FG-X distribution, which enhances the stiffness and load-bearing capacity of the plate more effectively than the other distributions. The table also demonstrates that as the system stiffness increases, due to higher Winkler and shear layer spring constant factors, the non-dimensional transverse displacement of CNTRC plates with Pasternak's elastic foundations decreases. Additionally, increasing the volume fraction of CNTs enhances the stiffness of the CNTRC plate for various CNTs distribution patterns. The higher CNT volume fraction increases the composite's overall rigidity, leading to a reduction in transverse displacement.

Table 4 Dimensionless deflection $\overline{w}\left(\frac{a}{2};\frac{b}{2};\frac{h}{2}\right)$ of CNTRC plate with and without elastic foundation

β_w	β_s		$V^*_{CNT}=0.11$				$V^*_{CNT}=0.14$				$V^*_{CNT}=0.17$			
			UD	X	O	V	UD	X	O	V	UD	X	O	V
0	0	Present	0.4963	0.4227	0.7080	0.5869	0.4395	0.3817	0.6147	0.5132	0.3176	0.2722	0.4525	0.3768
		TSDT [27]	0.4964	0.4227	0.7081	0.5869	0.4396	0.3817	0.6148	0.5133	0.3177	0.2723	0.4526	0.3769
		SSDT [27]	0.4953	0.4208	0.7104	0.5859	0.4383	0.3800	0.6168	0.5121	0.3170	0.2715	0.4537	0.3763
100	0	Present	0.4729	0.4055	0.6612	0.5543	0.4210	0.3676	0.5791	0.4882	0.3078	0.2651	0.4329	0.3631
		TSDT [27]	0.4729	0.4056	0.6612	0.5544	0.4210	0.3677	0.5792	0.4882	0.3079	0.2651	0.4330	0.3632
		SSDT [27]	0.4719	0.4038	0.6633	0.5534	0.4199	0.3661	0.5809	0.4872	0.3072	0.2644	0.4340	0.3626
100	50	Present	0.3224	0.2896	0.4001	0.3583	0.2974	0.2697	0.3685	0.3294	0.2361	0.2101	0.3033	0.2673
		TSDT [27]	0.3224	0.2896	0.4001	0.3583	0.2974	0.2698	0.3685	0.3295	0.2361	0.2101	0.3034	0.2674
		SSDT [27]	0.3219	0.2888	0.4009	0.3579	0.2969	0.2689	0.3692	0.3290	0.2357	0.2097	0.3039	0.2671

The non-dimensional transverse deflection of the CNTRC plate on a Pasternak elastic foundation is influenced by variations in the side-to-thickness ratio, as illustrated in Fig. 3. The study delves into non-dimensional transverse displacement variations across diverse CNT distributions, considering different thickness ratios and CNT volume fractions as 0.14 along with this the Winkler spring constant factors and shear layer spring constant factors set at 100 and 50, respectively. It scrutinizes FG-V, FG-O, FG-X, and UD distributions within the CNTRC plate. The analysis involves a square CNTRC plate with simple supported boundary conditions under sinusoidal loading, with findings expressed through a non-dimensional parameter specified in Eq. (26). Analysis indicates that among the UD, FG-V, and FG-O reinforcement distributions, the FG-X reinforcement distribution in the composite plate with a Pasternak's elastic foundation results in the minimal transverse deflection. This superior performance of the FG-X distribution can

be physically explained by the optimal gradation of CNTs, which enhances the stiffness and load-bearing capacity of the plate more effectively than other distributions. The FG-X distribution provides a more uniform distribution of stress and strain across the plate, thereby reducing localized bending and deformation. Additionally, the non-dimensional transverse displacement decreases with increasing system stiffness due to higher Winkler and shear layer spring constant factors. This behavior is due to the increased resistance provided by the stiffer foundation, which mitigates the bending and deflection of the plate under transverse loading. The stiffer foundation effectively supports the plate, distributing the load more evenly and reducing overall displacement.

The non-dimensional transverse deflection of the CNTRC plate on a Pasternak elastic foundation varies with the variations in the Winkler spring constant factors and shear layer spring constant factors, as depicted in Fig. 4. This study investigates the non-dimensional transverse displacement

Fig. 3 The effect of side to thickness ratio on non-dimensional transverse deflection $\overline{w}$ on CNTRC plate resting on the Pasternak's elastic foundation
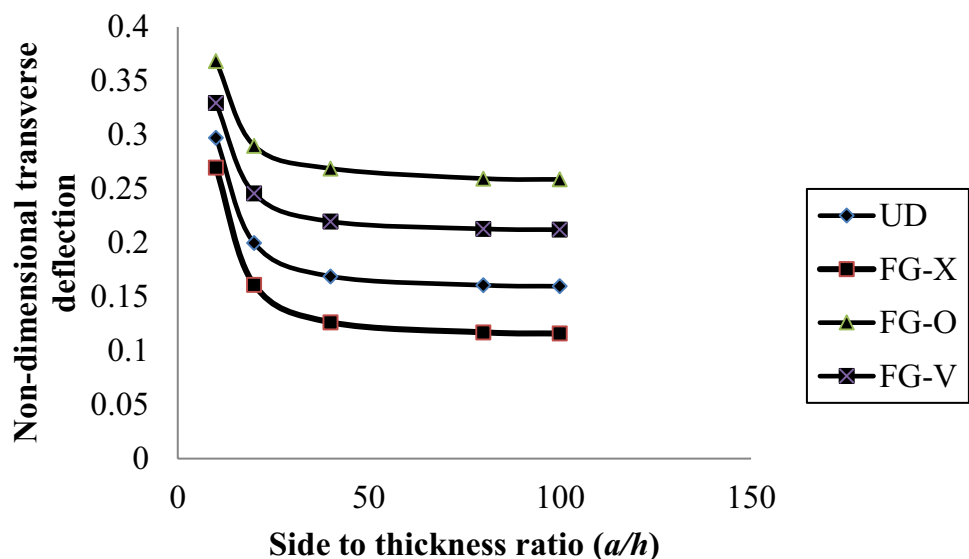
across different CNT distributions, considering thickness ratios as 10 and a CNT volume fraction of 0.17. The analysis examines FG-V, FG-O, FG-X, and UD distributions within the CNTRC plate. A square CNTRC plate with simply supported boundary conditions under sinusoidal loading is analyzed, with results presented using a non-dimensional parameter specified in Eq. (26). The figure shows that the non-dimensional transverse deflection of a CNTRC plate with a Pasternak's elastic foundation reduces when the Winkler spring constant factors and shear layer spring constant factors are increased, due to increase in the stiffness of the system. The higher CNT volume fraction increases the composite's overall rigidity, leading to a reduction in transverse displacement. This enhancement in stiffness is due to the superior mechanical properties of CNTs, which improve the

load-carrying capacity and structural integrity of the composite plate.

Figure 5 illustrates the effect of non-dimensional axial stress variation across the thickness of a CNTRC plate resting on a Pasternak's elastic foundation. This examines non-dimensional axial stress variations among different CNT distributions, considering span thickness ratios as 10 and CNTs volume fractions as 0.11 along with this Winkler and shear layer spring constants of 100 and 50, respectively. It analyzes FG-V, FG-O, FG-X, and UD distributions within CNTRC plates. The study focuses on a square CNTRC plate with simple supported boundary conditions under sinusoidal loading, presenting results via a non-dimensional parameter defined in Eq. (27). The figure reveals that the axial stress profile is symmetrical for symmetric CNT distribution

Fig. 4 The effect of different spring constant factors on non-dimensional transverse deflection $\overline{w}$ on CNTRC plate resting on the Pasternak's elastic foundation
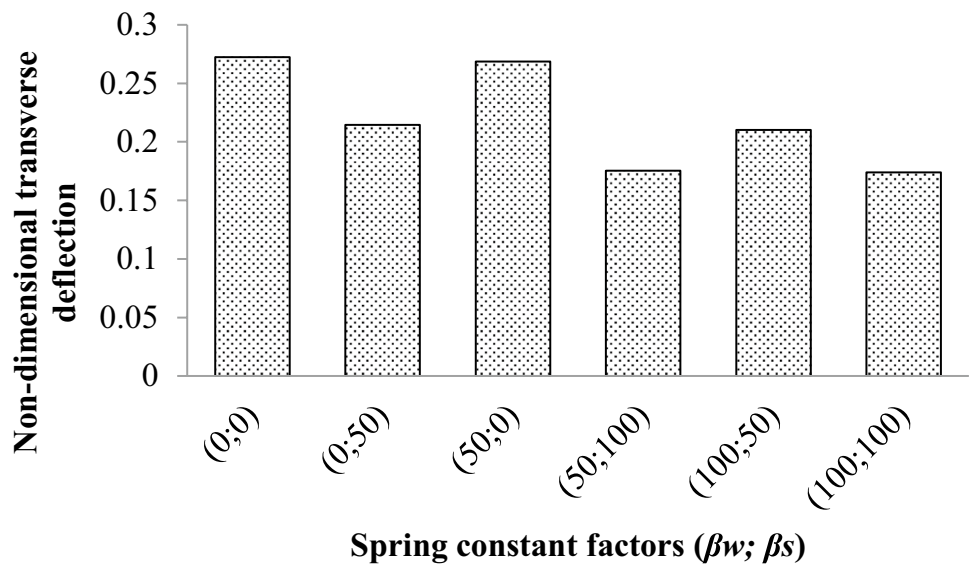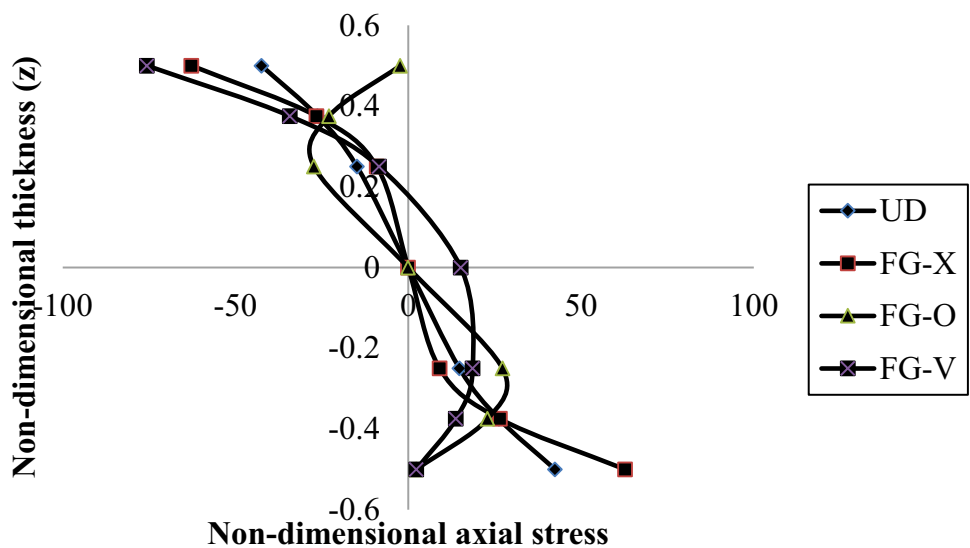

Fig. 5 The variation of non-dimensional axial stress $\bar{\sigma}_{xx}$ across the thickness of CNTRC plate resting on the Pasternak's elastic foundation for different distribution of CNTs

patterns, such as UD, FG-X, and FG-O, across the mid-plane of the plate. In contrast, it is asymmetrical for the FG-V distribution pattern. The distribution patterns of CNTs across the thickness significantly influence the axial stress variation. Specifically, the FG-V distribution shows the highest axial stress at the top of the plate, approaching zero at the bottom. Similarly, the FG-O distribution results in an axial stress profile that approaches zero at both the top and bottom of the plate due to minimal CNT concentration in these regions. At the midpoint of the CNTRC plate, the axial stress profile is zero for the UD, FG-X, and FG-O distributions but non-zero for the FG-V distribution. This behavior is due to the symmetrical CNT distribution in the UD, FG-X, and FG-O patterns, and the asymmetrical distribution in the FG-V pattern. These findings highlight the importance of CNT distribution patterns in influencing the stress response of CNTRC plates. The choice of distribution pattern can significantly affect the stress profile, which in turn impacts the overall structural performance and reliability of the composite plate.

Figure 6 depicts the variation of non-dimensional axial stress across the thickness of a CNTRC plate with FG-X CNT distribution, supported by a Pasternak's elastic foundation. The analysis is performed on a square CNTRC plate with simple supported boundary conditions under sinusoidal loading. Findings are reported using a non-dimensional parameter described in Eq. (27). The variation of non-dimensional axial stress across the thickness of a CNTRC plate under different Winkler and shear layer spring constant factors demonstrates that as the values of the Winkler and shear layer spring constant factors increase, the non-dimensional axial stress decreases. These findings highlight the significant role of foundation stiffness and CNT distribution patterns in influencing the stress response of CNTRC plates. By selecting appropriate foundation parameters and CNT

distributions, the structural performance and durability of CNTRC plates can be significantly improved.

Figure 7 presents the fluctuation of non-dimensional transverse shear stress across the thickness of the CNTRC plate resting on a Pasternak elastic foundation. The analysis considers a side-to-thickness ratio of 10 and various CNT dispersion patterns, with a CNT volume fraction of 0.14, and Winkler and shear layer spring constant values of 100 and 50, respectively. The analysis involves a square CNTRC plate with simple supported boundary conditions and sinusoidal loading. Findings are expressed using a non-dimensional parameter specified in Eq. (28). The figure reveals that the transverse shear stress profile is symmetrical for symmetric CNT distribution patterns, such as UD, FG-X, and FG-O, across the mid-plane of the plate, while it is asymmetrical for the FG-V distribution. The distribution of CNTs significantly affects the transverse shear stress variation across the thickness. The FG-O distribution exhibits the highest non-dimensional transverse shear stress, whereas the FG-X distribution shows the lowest. These findings highlight the importance of selecting appropriate CNT distribution patterns to optimize the shear stress response of CNTRC plates. The choice of distribution pattern can significantly influence the transverse shear stress profile, impacting the overall structural performance and reliability of the composite plate.

Buckling Analysis

This section goes into comprehensive detail on the buckling analysis of the CNTRC plate with Pasternak's elastic foundation under uniaxial and biaxial compressive stresses.

Table 5 presents the dimensionless critical buckling load of a CNTRC plate, both with and without a Pasternak's elastic foundation, under a uniaxial compressive load ($\Psi_x = -1$, $\Psi_y = 0$). This research focuses on the variations

Fig. 6 The variation of non-dimensional axial stress $\bar{\sigma}_{xx}$ across the thickness of CNTRC plate resting on the Pasternak's elastic foundation for FG-X CNTs distribution with different spring constant factors
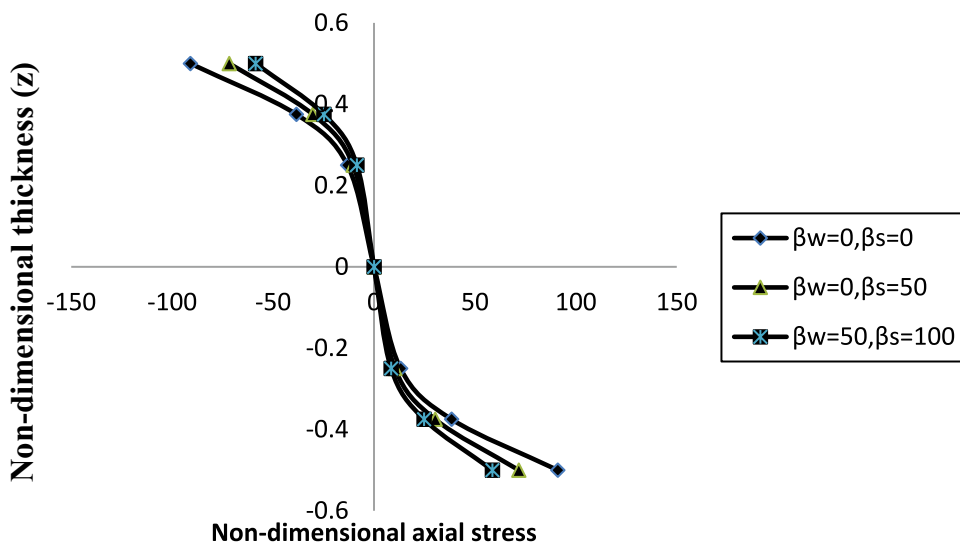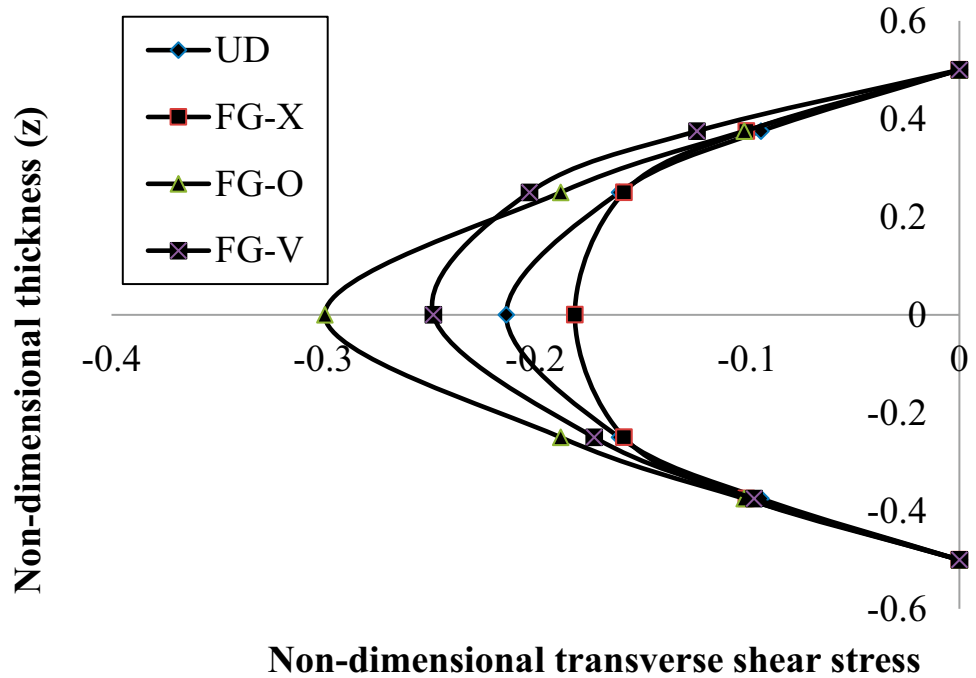
Fig. 7 The effect of variation of non-dimensional transverse shear stress $\overline{\tau}_{xz}$ across the thickness of CNTRC plate resting on the Pasternak's elastic foundation for different distribution of CNTs

in non-dimensional critical buckling load under a uniaxial compressive load ($\Psi_x = -1$, $\Psi_y = 0$) across different distributions of carbon nanotubes (CNTs), examining diverse thickness ratios and CNT volume fractions. The study scrutinizes FG-V, FG-O, and FG-X distributions, in addition to the UD distribution, within CNTRC plates. The analysis is conducted on a square CNTRC plate with simple supported boundary conditions subjected to sinusoidal loading. Results are reported using a non-dimensional parameter outlined in Eq. (31). The dimensionless critical buckling loads obtained are compared with those reported by Wattanasakulpong and Chaikittiratana [27], showing good agreement for a side-to-thickness ratio of 10. The table indicates that the FG-X CNT reinforcement distribution provides the

highest dimensionless critical buckling load under a uniaxial compressive load ($\Psi_x = -1$, $\Psi_y = 0$), followed by the UD and FG-O distributions, for both the CNTRC plate with and without the Pasternak's elastic foundation. The influence of the Winkler and shear layer spring constant factors is evident from the data due to which the lateral stiffness of the system increases due to higher Winkler and shear layer spring constant factors, the dimensionless critical buckling load under a uniaxial compressive load ($\Psi_x = -1$, $\Psi_y = 0$) also increases for the CNTRC plate with a Pasternak's elastic foundation. Similarly, increasing the volume fraction of CNTs enhances the stiffness and, consequently, the dimensionless critical buckling load. These findings highlight the importance of selecting appropriate CNT distribution

Table 5 Dimensionless critical buckling load $\overline{N}_{cr}$ under uniaxial compressive load ($\Psi_x = -1$, $\Psi_y = 0$) for CNTRC plate with and without elastic foundation

β_w	β_s		$V^*_{CNT} = 0.11$			$V^*_{CNT} = 0.14$			$V^*_{CNT} = 0.17$		
			UD	X	O	UD	X	O	UD	X	O
0	0	Present	20.6812	24.2858	14.4994	23.3556	26.8936	16.6988	32.3177	37.6938	22.6828
		TSDT [27]	20.6814	24.2864	14.4990	22.3559	26.8941	16.6984	32.3180	37.6944	22.6823
		SSDT [27]	20.7286	24.3943	14.4515	23.4229	27.0177	16.6451	32.3890	37.8069	22.6276
100	0	Present	21.7078	25.3424	15.5260	24.3822	27.9200	17.7254	33.3443	38.7204	23.7094
		TSDT [27]	21.7080	25.3130	15.5256	24.3825	27.9207	17.7250	33.3446	38.7210	23.7089
		SSDT [27]	21.7552	25.4209	15.4781	24.4495	28.0443	17.6717	33.4156	38.8335	23.6542
100	50	Present	31.8399	34.4445	25.6581	34.5143	38.0521	27.8576	43.4764	48.8525	33.8415
		TSDT [27]	31.8401	35.4451	25.6577	34.5146	38.0528	27.8571	43.4768	48.8531	33.8410
		SSDT [27]	31.8873	35.5531	25.6102	34.5816	38.1764	27.8038	43.5477	48.9656	33.7863

patterns and foundation stiffness parameters to optimize the buckling resistance of CNTRC plates. The choice of distribution pattern and foundation parameters can significantly influence the critical buckling load, impacting the overall structural performance and reliability of the composite plate.

Table 6 shows the dimensionless critical buckling load under a biaxial compressive load ($\Psi_x = -1$, $\Psi_y = -1$). This analysis explores non-dimensional critical buckling load under a biaxial compressive load variation among various distributions of carbon nanotubes (CNTs), considering different thickness ratios and CNT volume fractions. FG-V, FG-O, and FG-X distributions, as well as UD distribution, are examined within the framework of CNTRC plates. The study focuses on a square CNTRC plate with simple supported boundary conditions under sinusoidal loading, presenting results through a non-dimensional parameter described in Eq. (31). Again, the results are compared with those of Wattanasakulpong and Chaikittiratana [27], and the agreement is satisfactory. A comparison of Tables 5 and 6 reveals that the dimensionless critical buckling loads under biaxial compressive loading are lower than those under uniaxial compressive loading for the same CNT volume fractions, distribution patterns, and spring constant factors. These findings underscore the importance of selecting appropriate CNT distribution patterns and foundation stiffness parameters to optimize the buckling resistance of CNTRC plates under various loading conditions. The choice of distribution pattern and foundation parameters can significantly influence the critical buckling load, impacting the overall structural performance and reliability of the composite plate.

Figure 8 illustrates the effect of varying the Winkler and shear layer spring constant factors on the non-dimensional critical buckling load of a CNTRC plate with a Pasternak's elastic foundation with UD reinforcement distribution. The
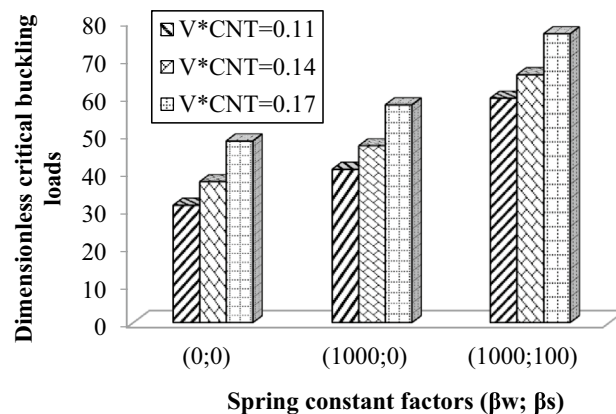

Fig. 8 Effect of different spring constant factors on non-dimensional critical buckling load under uni-axial loading $\overline{N}_{cr}$ ($\Psi_x = -1$, $\Psi_y = 0$) condition for different volume fraction of CNTs on CNTRC plate resting on the Pasternak's elastic foundation

analysis involves a square CNTRC plate with simple supported boundary conditions and sinusoidal loading. Findings are expressed using a non-dimensional parameter specified in Eq. (31). The analysis includes different Winkler and shear layer spring constant factors and CNT volume fractions. The figure shows that for a given CNT volume fraction, the non-dimensional critical buckling load increases with the values of the Winkler and shear layer spring constant factors. In composite structures like CNTRC plates, the foundation stiffness plays a crucial role in resisting buckling under compressive loads. Higher values of the Winkler and shear layer spring constants result in a stiffer support system beneath the plate. This increased stiffness effectively distributes and absorbs the compressive forces applied to the plate, thereby increasing its buckling resistance. Essentially, the stiffer foundation reduces the magnitude of deformations that

Table 6 Dimensionless critical buckling load $\overline{N}_{cr}$ under bi axial compressive load ($\Psi_x = -1$, $\Psi_y = -1$) for CNTRC plate with and without elastic foundation

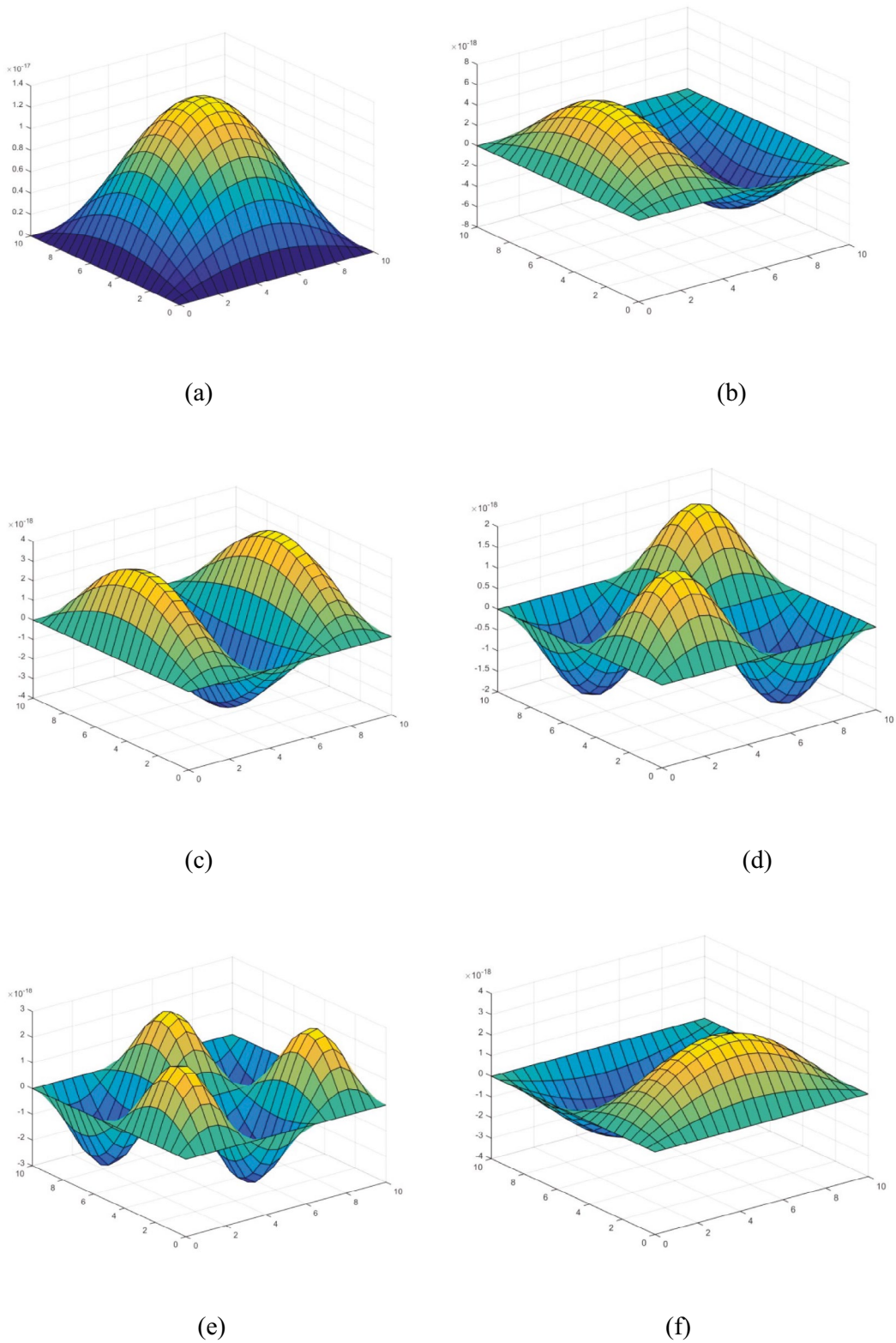| β_w	β_s		$V^*_{CNT} = 0.11$			$V^*_{CNT} = 0.14$			$V^*_{CNT} = 0.17$		
			UD	X	O	UD	X	O	UD	X	O
0	0	Present	10.3406	12.1429	7.2497	11.6788	13.4467	8.3494	16.1588	18.8469	11.3414
		TSDT [27]	10.3407	12.1432	7.2495	11.6780	13.4471	8.3492	16.1590	18.8472	11.3412
		SSDT [27]	10.3643	12.1972	7.2257	11.7115	13.5089	8.3225	16.1945	18.9035	11.3138
100	0	Present	10.8539	12.6562	7.7630	12.1911	13.9600	8.8627	16.6721	19.3602	11.8547
		TSDT [27]	10.8540	12.6565	7.7628	12.1913	13.9604	8.8625	16.6723	19.3605	11.8544
		SSDT [27]	10.8776	12.7105	7.7390	12.2248	14.0222	8.8358	16.7078	19.4168	11.8271
100	50	Present	15.9199	17.7222	12.8291	17.2571	19.0261	13.9288	21.7382	24.4263	16.9208
		TSDT [27]	15.9201	17.72260	12.8289	17.2573	19.0264	13.9285	21.7384	24.4265	16.9205
		SSDT [27]	15.9437	17.7765	12.8051	17.2980	19.0882	13.9019	21.7739	24.4828	16.8931

(a)

(b)

(c)

(d)

(e)

(f)

Fig. 9 First six mode shapes of simply supported CNTRC plate resting on the Pasternak's elastic foundation for buckling loads $\overline{N}_{cr}$

Table 7 Dimensionless natural frequency $\overline{\omega}$ for CNTRC plate with and without elastic foundation

β_w	β_s		$V^*_{CNT}=0.11$				$V^*_{CNT}=0.14$				$V^*_{CNT}=0.17$			
			UD	X	O	V	UD	X	O	V	UD	X	O	V
0	0	Present	0.1355	0.1469	0.1134	0.1245	0.1436	0.1541	0.1213	0.1328	0.1683	0.1819	0.1409	0.1544
		TSDT [27]	0.1355	0.1469	0.1134	0.1245	0.1436	0.1541	0.1213	0.1328	0.1683	0.1819	0.1409	0.1544
		SSDT [27]	0.1357	0.1472	0.1132	0.1246	0.1438	0.1545	0.1211	0.1329	0.1685	0.1821	0.1408	0.1546
100	0	Present	0.1388	0.1500	0.1173	0.1281	0.1467	0.1570	0.1250	0.1362	0.1710	0.1443	0.1441	0.1573
		TSDT [27]	0.1388	0.1500	0.1173	0.1281	0.1467	0.1570	0.1250	0.1362	0.1710	0.1443	0.1441	0.1573
		SSDT [27]	0.1390	0.1503	0.1172	0.1282	0.1469	0.1574	0.1248	0.1363	0.1712	0.1846	0.1439	0.1574
100	50	Present	0.1683	0.1775	0.1509	0.1594	0.1746	0.1833	0.1567	0.1657	0.1953	0.2070	0.1721	0.1834
		TSDT [27]	0.1683	0.1775	0.1509	0.1594	0.1746	0.1833	0.1567	0.1657	0.1953	0.2070	0.1721	0.1834
		SSDT [27]	0.1683	0.1777	0.1507	0.1595	0.1747	0.1836	0.1566	0.1659	0.1954	0.2073	0.1720	0.1835

could lead to instability, thereby raising the critical buckling load. Similarly, for a given set of spring constant factors, the non-dimensional critical buckling load increases with the CNT volume fraction. This phenomenon occurs because higher CNT volume fractions enhance the overall stiffness and strength of the CNTRC plate. The increased stiffness provided by a higher volume fraction of CNTs allows the plate to withstand higher compressive loads before buckling occurs, thereby increasing the critical buckling load.

Figure 9 depicts the first six buckling mode shapes of a simply supported CNTRC plate on a Pasternak's elastic foundation, focusing on the FG-X distribution of CNTs. The analysis is conducted on a square CNTRC plate with simple supported boundary conditions subjected to sinusoidal loading. Results are reported using a non-dimensional parameter outlined in Eq. (31). The mode shapes are constructed for a CNT volume fraction of 0.17 and a side-to-thickness ratio of 10, with shear layer spring constant factors of 50 and 100, respectively, for the Winkler spring constant factors. This phenomenon arises because the FG-X distribution effectively reinforces the plate, distributing compressive forces more evenly and resisting buckling across its surface.
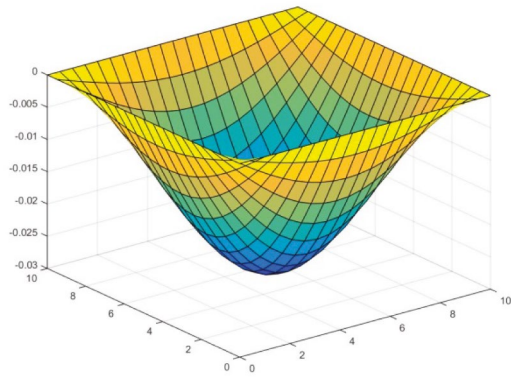
Free Vibration Analysis

This section goes into extensive detail on the free vibration analysis of the CNTRC plate with Pasternak's elastic foundation.

Table 7 presents the dimensionless natural frequency of the CNTRC plate with and without a Pasternak's elastic foundation. This study explores the dimensionless natural frequency of CNTRC plates across various CNT volume fractions, CNT distribution patterns, and spring constant factors. The FG-V, FG-O, and FG-X distributions, along with the UD distribution, are specifically analyzed in the context of CNTRC plate with and without a Pasternak's elastic foundation. The analysis focuses on a square CNTRC plate with simple supported boundary conditions. The findings

are presented using a non-dimensional parameter as defined by Eq. (30). The results obtained align closely with those reported by Wattanasakulpong and Chaikittiratana [27]. For a side-to-thickness ratio of 10, the dimensionless natural frequency is computed for CNTRC plates both with and without the Pasternak elastic foundation. The table reveals that the FG-X reinforcement distribution of CNTs yields the highest natural frequency, followed by the UD, FG-V, and FG-O distributions. This trend can be explained by the superior mechanical properties imparted by the FG-X distribution, which optimally reinforces the plate against deformation and enhances its stiffness. As a result, the plate exhibits higher natural frequencies due to increased rigidity and reduced mass per unit area, leading to faster vibration cycles. The data indicate that the dimensionless natural frequency increases with higher Winkler spring constant factors and shear layer spring constant factors for the CNTRC plate with a Pasternak elastic foundation. Additionally, increasing the CNT volume fraction enhances the dimensionless natural frequency across different CNT distribution patterns. Additionally, increasing the CNT volume fraction enhances the dimensionless natural frequency across different distribution patterns. Higher volume fractions improve the overall stiffness and strength of the CNTRC plate, resulting in higher natural frequencies due to enhanced structural integrity and reduced deformation under vibrational modes.

Figure 10 illustrates the first six mode shapes of the natural frequency for a simply supported CNTRC plate on a Pasternak elastic foundation. The mode shapes are depicted for an FG-O CNT distribution with a CNT volume fraction of 0.14 and a side-to-thickness ratio of 10. The shear layer spring constant factors and Winkler spring constant factors are set at 50 and 100, respectively. The mode shapes represent distinct vibrational patterns exhibited by the CNTRC plate under natural frequency conditions. Each mode shape corresponds to a specific vibration mode and frequency, characterized by the spatial distribution of displacements across the plate.
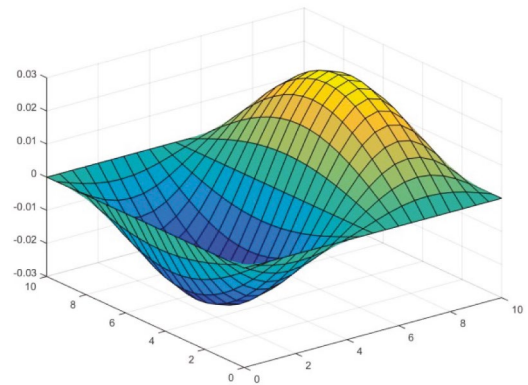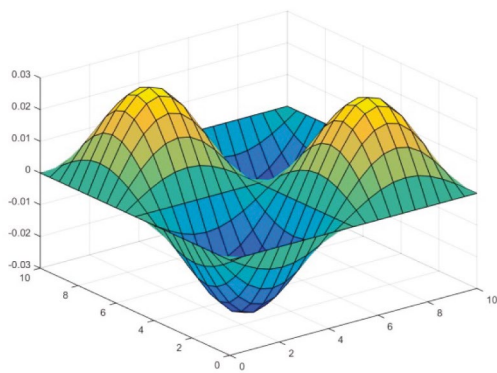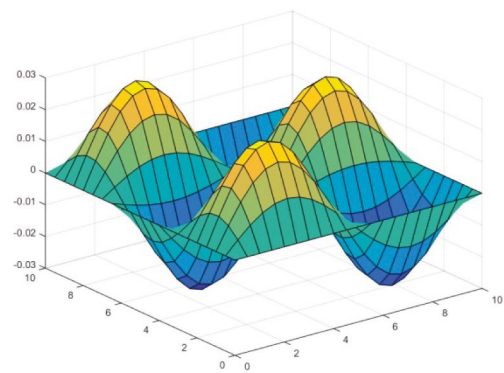
(a)
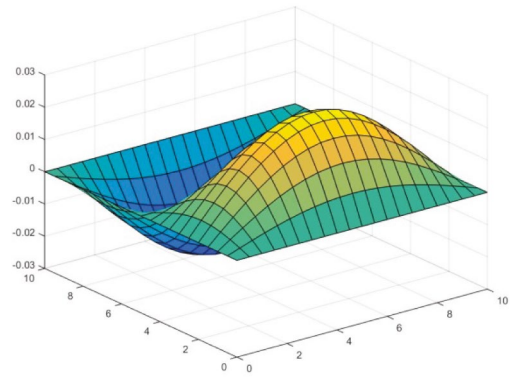
(b)
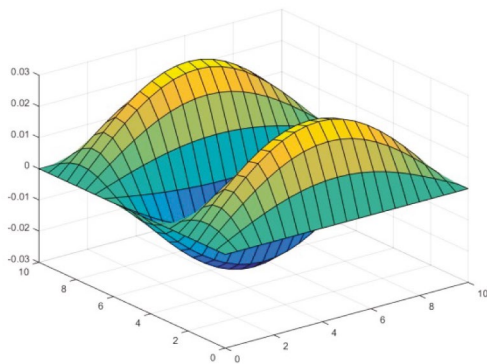
(c)

(d)

(e)

(f)

Fig. 10 First six mode shapes of simply supported CNTRC plate resting on the Pasternak's elastic foundation for free vibration $\overline{\omega}$

Conclusions

The secant function-based non polynomial shear deformation theory (SDTSF) is employed to analyze the bending, buckling, and free vibration behaviors of a CNTRC plate resting on a Pasternak's elastic foundation. This foundation model includes Winkler spring and shear layer components, which are fundamental to Pasternak's elastic theory. The equation of motion for the CNTRC plate with a Pasternak elastic foundation is derived using Hamilton's principle and solved using Navier's solution method. The static analysis reveals that the FG-X reinforcement distribution of CNTs in the composite plate with the Pasternak's elastic foundation effectively minimizes transverse deflection, whereas the FG-O distribution results in the maximum transverse deflection. By adjusting the CNTs volume fraction, Winkler spring constant factors, and shear layer spring constant factors, the stiffness of the CNTRC plate can be optimized for various CNT distribution patterns. Axial stress and transverse shear stress profiles are found to be symmetrical for UD, FG-X, and FG-O CNT distribution patterns across the mid-plane of the plate, but asymmetrical for the FG-V pattern. Among the different distribution patterns, the FG-O distribution exhibits the highest non-dimensional transverse shear stress, while the FG-X distribution shows the lowest. Buckling analysis indicates that the FG-X reinforcement distribution of CNTs in the composite plate with the Pasternak elastic foundation achieves the highest dimensionless critical buckling load, followed by the UD and FG-O distributions. The FG-X distribution also results in the highest natural frequency, followed by UD, FG-V, and FG-O distributions. Increasing the volume fraction of CNTs, Winkler spring constant factors, and shear layer spring constant factors enhances the buckling and free vibration responses of CNTRC plates with Pasternak elastic foundations. However, the current study has some limitations that future work should address. The present analysis is restricted to simply supported boundary conditions, and extending it to other boundary conditions could provide a more comprehensive understanding of CNTRC plate behavior. Additionally, while this study considers static, buckling, and free vibration behavior, the effects of dynamic loading and thermal environments remain unexplored and warrant further investigation. Future studies could also incorporate more complex loading scenarios and explore the long-term durability and performance of CNTRC plates in real-world applications.

Appendix A

Partial differential equation terms of the primary variables are separated for different displacement modes derived at the mid plane are shown below:

$$
\begin{aligned}
& A_{11}\left(\frac{\partial^2 u_0}{\partial x^2}\right) + B_{11}\left(\Omega\frac{\partial^2 \theta_x}{\partial x^2} - \frac{\partial^3 w_0}{\partial x^3}\right) + E_{11}\left(\frac{\partial^2 \theta_x}{\partial x^2}\right) \\
& + A_{12}\left(\frac{\partial^2 v_0}{\partial x \partial y}\right) + B_{12}\left(\Omega\frac{\partial^2 \theta_y}{\partial x \partial y} - \frac{\partial^3 w_0}{\partial x \partial y^2}\right) + E_{12}\left(\frac{\partial^2 \theta_y}{\partial x \partial y}\right) \\
& + A_{66}\left(\frac{\partial^2 u_0}{\partial y^2} + \frac{\partial^2 v_0}{\partial x \partial y}\right) - B_{66}\left(\Omega\left(\frac{\partial^2 \theta_x}{\partial y^2} + \frac{\partial^2 \theta_y}{\partial x \partial y}\right) - 2\frac{\partial^3 w_0}{\partial x \partial y^2}\right) \\
& + E_{66}\left(\frac{\partial^2 \theta_x}{\partial y^2} + \frac{\partial^2 \theta_y}{\partial x \partial y}\right) = I_0\ddot{u} - +I_1\frac{\partial \ddot{w}_0}{\partial x} + I_3\ddot{\theta}_x
\end{aligned} \tag{A1}
$$

$$
\begin{aligned}
& B_{11}\left(\frac{\partial^3 u_0}{\partial x^3}\right) + D_{11}\left(\Omega\frac{\partial^3 \theta_x}{\partial x^3} - \frac{\partial^4 w_0}{\partial x^4}\right) + F_{11}\left(\frac{\partial^3 \theta_x}{\partial x^3}\right) + B_{12}\left(\frac{\partial^3 u_0}{\partial x \partial y^2} + \frac{\partial^2 v_0}{\partial x^2 \partial y}\right) \\
& + B_{22}\left(\frac{\partial^3 v_0}{\partial y^3}\right) + D_{12}\left(\Omega\left(\frac{\partial^3 \theta_x}{\partial y^2 \partial x} + \frac{\partial^3 \theta_y}{\partial x^2 \partial y}\right) - 2\frac{\partial^4 w_0}{\partial x^2 \partial y^2}\right) \\
& + F_{12}\left(\frac{\partial^3 \theta_y}{\partial x^2 \partial y} + \frac{\partial^3 \theta_x}{\partial x \partial y^2}\right) + D_{22}\left(\Omega\frac{\partial^3 \theta_y}{\partial y^3} - \frac{\partial^4 w_0}{\partial y^4}\right) + F_{22}\left(\frac{\partial^3 \theta_y}{\partial y^3}\right) \\
& + 2B_{66}\left(\frac{\partial^3 u_0}{\partial x \partial y^2} + \frac{\partial^3 v_0}{\partial x^2 \partial y}\right) - 2D_{66}\left(\Omega\left(\frac{\partial^3 \theta_x}{\partial x \partial y^2} + \frac{\partial^3 \theta_y}{\partial x^2 \partial y}\right) - 2\frac{\partial^4 w_0}{\partial x^2 \partial y^2}\right) \\
& + 2F_{66}\left(\frac{\partial^3 \theta_x}{\partial x \partial y^2} + \frac{\partial^3 \theta_y}{\partial x^2 \partial y}\right) \\
& = I_1\left(\frac{\partial \ddot{u}_0}{\partial x} + \frac{\partial \ddot{v}_0}{\partial y}\right) - I_2\left(\frac{\partial^2 \ddot{w}_0}{\partial x^2} + \frac{\partial^2 \ddot{w}_0}{\partial y^2}\right) + I_4\left(\frac{\partial \ddot{\theta}_x}{\partial x} + \frac{\partial \ddot{\theta}_y}{\partial y}\right) + I_0\ddot{w}_0
\end{aligned} \tag{A2}
$$

$$
\begin{aligned}
& A_{12}\left(\frac{\partial^2 u_0}{\partial x \partial y}\right) + B_{12}\left(\Omega\frac{\partial^2 \theta_x}{\partial x \partial y} - \frac{\partial^3 w_0}{\partial x^2 \partial y}\right) + E_{12}\left(\frac{\partial^2 \theta_x}{\partial x \partial y}\right) \\
& + A_{22}\left(\frac{\partial^2 v_0}{\partial y^2}\right) + B_{22}\left(\Omega\frac{\partial^2 \theta_y}{\partial y^2} - \frac{\partial^3 w_0}{\partial y^3}\right) + E_{22}\left(\frac{\partial^2 \theta_y}{\partial y^2}\right) \\
& + A_{66}\left(\frac{\partial^2 u_0}{\partial x \partial y} + \frac{\partial^2 v_0}{\partial x^2}\right) - B_{66}\left(\Omega\left(\frac{\partial^2 \theta_x}{\partial x \partial y} + \frac{\partial^2 \theta_y}{\partial x^2}\right) - 2\frac{\partial^3 w_0}{\partial x^2 \partial y}\right) \\
& + E_{66}\left(\frac{\partial^2 \theta_x}{\partial x \partial y} + \frac{\partial^2 \theta_y}{\partial x^2}\right) + q - k_w w_0 + k_s\frac{\partial^2 w_0}{\partial x^2} \\
& + k_s\frac{\partial^2 w_0}{\partial y^2} + \overline{N}_{xx}\frac{\partial^2 w_0}{\partial x^2} + 2\overline{N}_{xy}\frac{\partial^2 w_0}{\partial x \partial y} + \overline{N}_{yy}\frac{\partial^2 w_0}{\partial y^2} \\
& = I_0\ddot{v}_0 + I_1\frac{\partial \ddot{w}_0}{\partial y} + I_3\ddot{\theta}_y
\end{aligned} \tag{A3}
$$

$$(\Omega B_{11} + E_{11})\left(\frac{\partial^2 u_0}{\partial x^2}\right) + (\Omega D_{11} + F_{11})\left(\Omega\frac{\partial^2 \theta_x}{\partial x^2} - \frac{\partial^3 w_0}{\partial x^3}\right)$$
$$+ (\Omega F_{11} + H_{11})\left(\frac{\partial^2 \theta_x}{\partial x^2}\right) + (\Omega B_{66} + E_{66})\left(\frac{\partial^2 u_0}{\partial y^2} + \frac{\partial^2 v_0}{\partial x \partial y}\right)$$
$$+ (\Omega B_{12} + E_{12})\left(\frac{\partial^2 v_0}{\partial x \partial y}\right) + (\Omega F_{12} + H_{12})\left(\frac{\partial^2 \theta_y}{\partial x \partial y}\right)$$
$$+ (\Omega D_{12} + F_{12})\left(\Omega\frac{\partial^2 \theta_y}{\partial y \partial x} + \frac{\partial^3 w_0}{\partial x \partial y^2}\right)$$
$$+ (\Omega F_{66} + H_{66})\left(\frac{\partial^2 \theta_x}{\partial y^2} + \frac{\partial^2 \theta_y}{\partial x \partial y}\right)$$
$$+ (\Omega D_{66} + F_{66})\left(\Omega\left(\frac{\partial^2 \theta_x}{\partial y^2} + \frac{\partial^2 \theta_y}{\partial x \partial y}\right) - 2\frac{\partial^3 w_0}{\partial x \partial y^2}\right)$$
$$- [\Omega^2 A_{55} + 2\Omega K_{55} + L_{55}]\theta_x = I_3 \ddot{u}_0 - I_4 \frac{\partial w_0}{\partial x} + I_5 \ddot{\theta}_x$$
$$\tag{A4}$$

$$(\Omega B_{12} + E_{12})\left(\frac{\partial^2 u_0}{\partial x \partial y}\right) + (\Omega D_{12} + F_{12})\left(\Omega\frac{\partial^2 \theta_x}{\partial x \partial y} - \frac{\partial^3 w_0}{\partial x^2 \partial y}\right)$$
$$+ (\Omega F_{12} + H_{12})\left(\frac{\partial^2 \theta_x}{\partial x \partial y}\right) + (\Omega B_{66} + E_{66})\left(\frac{\partial^2 u_0}{\partial x \partial y} + \frac{\partial^2 v_0}{\partial x^2}\right)$$
$$+ (\Omega B_{22} + E_{22})\left(\frac{\partial^2 v_0}{\partial y^2}\right) + (\Omega F_{22} + H_{22})\left(\frac{\partial^2 \theta_y}{\partial y^2}\right)$$
$$+ (\Omega D_{22} + F_{22})\left(\Omega\frac{\partial^2 \theta_y}{\partial y^2} + \frac{\partial^3 w_0}{\partial y^3}\right) + (\Omega F_{66} + H_{66})\left(\frac{\partial^2 \theta_x}{\partial x \partial y} + \frac{\partial^2 \theta_y}{\partial x^2}\right)$$
$$+ (\Omega D_{66} + F_{66})\left(\Omega\left(\frac{\partial^2 \theta_x}{\partial x \partial y} + \frac{\partial^2 \theta_y}{\partial x^2}\right) - 2\frac{\partial^3 w_0}{\partial x^2 \partial y}\right)$$
$$- [\Omega^2 A_{44} + 2\Omega K_{44} + L_{44}]\theta_y = I_3 \ddot{v}_0 - I_4 \frac{\partial w_0}{\partial y} + I_5 \ddot{\theta}_y$$
$$\tag{A5}$$

Appendix B: Coefficient of Mass Matrix

$$
\begin{aligned}
&M_{11} = -I_0, \ M_{13} = I_1 a, \ M_{14} = -I_3, \\
&M_{22} = -I_0, \ M_{23} = I_1 b, \ M_{25} = -I_3 \\
&M_{33} = -I_0 - I_2(a^2 + b^2), \ M_{34} = I_4 a, \\
&M_{35} = I_4 b, \ M_{44} = M_{55} = -I_5
\end{aligned}
\tag{B1}
$$

Data availability The raw/processed data required to reproduce these findings cannot be shared at this time as the data also forms part of an ongoing study.

Declarations

Conflict of interest The author(s) declare(s) that there is no conflict of interest regarding the publication of this paper.

References

1. Lau AKT, Hui D (2002) The revolutionary creation of new advanced materials—carbon nanotube composites. Composites B Engineering 33(4):263–277
2. Thostenson ET, Ren Z, Chou TW (2001) Advances in the science and technology of carbon nanotubes and their composites: a review. Compos Sci Technol 61(13):1899–1912
3. Saito Y, Hamaguchi K, Hata K, Uchida K, Tasaka Y, Ikazaki F, Nishina Y (1997) Conical beams from open nanotubes. Nature 389(6651):554–555
4. Niu C, Sichel EK, Hoch R, Moy D, Tennent H (1997) High power electrochemical capacitors based on carbon nanotube electrodes. Appl Phys Lett 70(11):1480–1482
5. Vaccarini L, Goze C, Henrard L, Hernandez E, Bernier P, Rubio A (2000) Mechanical and electronic properties of carbon and boron–nitride nanotubes. Carbon 38(11–12):1681–1690
6. Iijima S (1991) Helical microtubules of graphitic carbon. Nature 354(6348):56–58
7. Overney G, Zhong W, Tomanek D (1993) Structural rigidity and low frequency vibrational modes of long carbon tubules. Z Phys D 27(1):93–96
8. Wong EW, Sheehan PE, Lieber CM (1997) Nanobeam mechanics: elasticity, strength, and toughness of nanorods and nanotubes. Science 277(5334):1971–1975
9. Iijima S, Ichihashi T (1993) Single-shell carbon nanotubes of 1-nm diameter. Nature 363(6430):603–605
10. Bethune DS, Kiang CH, De Vries MS, Gorman G, Savoy R, Vazquez J, Beyers R (1993) Cobalt-catalysed growth of carbon nanotubes with single-atomic-layer walls. Nature 363(6430):605–607
11. Kelly BT (1982) Graphite—the most fascinating nuclear material. Carbon 20(1):3–11
12. Liew KM, Pan Z, Zhang LW (2020) The recent progress of functionally graded CNT reinforced composites and structures. Sci China Phys Mech Astron 63(3):1–17
13. Liew KM, Pan ZZ, Zhang LW (2019) An overview of layerwise theories for composite laminates and structures: development, numerical implementation and application. Compos Struct 216:240–259
14. Yengejeh SI, Kazemi SA, Öchsner A (2017) Carbon nanotubes as reinforcement in composites: a review of the analytical, numerical and experimental approaches. Comput Mater Sci 136:85–101
15. Khaniki HB, Ghayesh MH (2020) A review on the mechanics of carbon nanotube strengthened deformable structures. Eng Struct 220:110711
16. Ajayan PM, Stephan O, Colliex C, Trauth D (1994) Aligned carbon nanotube arrays formed by cutting a polymer resin-nanotube composite. Science 265:1212–1214
17. Odegard GM, Gates TS, Wise KE, Park C, Siochi EJ (2003) Constitutive modeling of nanotube–reinforced polymer composites. Compos Sci Technol 63(11):1671–1687
18. Griebel M, Hamaekers J (2004) Molecular dynamics simulations of the elastic moduli of polymer–carbon nanotube composites. Comput Methods Appl Mech Eng 193(17–20):1773–1788
19. Mokashi VV, Qian D, Liu Y (2007) A study on the tensile response and fracture in carbon nanotube-based composites using molecular mechanics. Compos Sci Technol 67(3–4):530–540
20. Wattanasakulpong N, Ungbhakorn V (2013) Analytical solutions for bending, buckling and vibration responses of carbon nanotube-reinforced composite beams resting on elastic foundation. Comput Mater Sci 71:201–208
21. Yas MH, Samadi N (2012) Free vibrations and buckling analysis of carbon nanotube-reinforced composite Timoshenko beams on elastic foundation. Int J Press Vessels Pip 98:119–128

22. Shen HS, Xiang Y (2013) Nonlinear analysis of nanotube-reinforced composite beams resting on elastic foundations in thermal environments. Eng Struct 56:698–708

23. Shen HS, Xiang Y (2014) Nonlinear bending of nanotube-reinforced composite cylindrical panels resting on elastic foundations in thermal environments. Eng Struct 80:163–172

24. Shen HS, Xiang Y (2014) Nonlinear vibration of nanotube-reinforced composite cylindrical panels resting on elastic foundations in thermal environments. Compos Struct 111:291–300

25. Zhang LW, Lei ZX, Liew KM (2015) An element-free IMLS-Ritz framework for buckling analysis of FG–CNT reinforced composite thick plates resting on Winkler foundations. Eng Anal Bound Elem 58:7–17

26. Zhang LW, Song ZG, Liew KM (2015) Nonlinear bending analysis of FG-CNT reinforced composite thick plates resting on Pasternak foundations using the element-free IMLS-Ritz method. Compos Struct 128:165–175

27. Wattanasakulpong N, Chaikittiratana A (2015) Exact solutions for static and dynamic analyses of carbon nanotube-reinforced composite plates with Pasternak elastic foundation. Appl Math Model 39(18):5459–5472

28. Lei ZX, Zhang LW, Liew KM (2015) Buckling of FG-CNT reinforced composite thick skew plates resting on Pasternak foundations based on an element-free approach. Appl Math Comput 266:773–791

29. Lei ZX, Zhang LW, Liew KM (2016) Vibration of FG-CNT reinforced composite thick quadrilateral plates resting on Pasternak foundations. Eng Anal Bound Elem 64:1–11

30. Zhang LW, Liew KM (2015) Large deflection analysis of FG-CNT reinforced composite skew plates resting on Pasternak foundations using an element-free approach. Compos Struct 132:974–983

31. Mohammadzadeh-Keleshteri M, Asadi H, Aghdam MM (2017) Geometrical nonlinear free vibration responses of FG-CNT reinforced composite annular sector plates integrated with piezoelectric layers. Compos Struct 171:100–112

32. Kutlu A, Omurtag MH (2012) Large deflection bending analysis of elliptic plates on orthotropic elastic foundation with mixed finite element method. Int J Mech Sci 65(1):64–74

33. Duc ND, Cong PH, Tuan ND, Tran P, Van Thanh N (2017) Thermal and mechanical stability of functionally graded carbon nanotubes (FG CNT)-reinforced composite truncated conical shells surrounded by the elastic foundations. Thin-Walled Struct 115:300–310

34. Ansari R, Torabi J, Faghih Shojaei M (2018) Free vibration analysis of embedded functionally graded carbon nanotube-reinforced composite conical/cylindrical shells and annular plates using a numerical approach. J Vib Control 24(6):1123–1144

35. Van Tham V, Huu Quoc T, Minh Tu T (2019) Free vibration analysis of laminated functionally graded carbon nanotube-reinforced composite doubly curved shallow shell panels using a new four-variable refined theory. J Compos Sci 3(4):104

36. Truong-Thi T, Vo-Duy T, Ho-Huu V, Nguyen-Thoi T (2020) Static and free vibration analyses of functionally graded carbon nanotube reinforced composite plates using CS-DSG3. Int J Comput Methods 17(03):1850133

37. Zghal S, Frikha A, Dammak F (2018) Free vibration analysis of carbon nanotube-reinforced functionally graded composite shell structures. Appl Math Model 53:132–155

38. Forooghi A, Fallahi N, Alibeigloo A, Forooghi H, Rezaey S (2023) Static and thermal instability analysis of embedded functionally graded carbon nanotube-reinforced composite plates based on HSDT via GDQM and validated modeling by neural network. Mech Based Des Struct Mach 51(12):7149–7182

39. Thai CH, Tran TD, Phung-Van P (2020) A size-dependent moving Kriging meshfree model for deformation and free vibration analysis of functionally graded carbon nanotube-reinforced composite nanoplates. Eng Anal Bound Elem 115:52–63

40. Thai CH, Ferreira AJM, Tran TD, Phung-Van P (2019) Free vibration, buckling and bending analyses of multilayer functionally graded graphene nanoplatelets reinforced composite plates using the NURBS formulation. Compos Struct 220:749–759

41. Daikh AA, Houari MSA, Belarbi MO, Mohamed SA, Eltaher MA (2022) Static and dynamic stability responses of multilayer functionally graded carbon nanotubes reinforced composite nanoplates via quasi 3D nonlocal strain gradient theory. Defence Technol 18(10):1778–1809

42. Sharma LK, Grover N, Bhardwaj G (2023) Buckling and free vibration analysis of temperature-dependent functionally graded CNT-reinforced plates. J Vib Eng Technol 11(1):175–192

43. Uymaz B, Uymaz G (2024) Three-dimensional thermal vibration of CFFF functionally graded carbon nanotube-reinforced composite plates. J Vib Eng Technol 12(4):5345–5368

44. Li PQ, Wang KF, Wang BL (2024) Nonlinear vibration of the sandwich beam with auxetic honeycomb core under thermal shock. Thin-Walled Struct 196:111479

45. Zhang Z, Wang Y, Zhang W (2023) Temperature-and moisture-dependent aeroelastic stability of graphene platelet reinforced nanocomposite lattice sandwich plates subjected to supersonic flow. Aerosp Sci Technol 138:108348

46. Wang Y, Zhang Z, Zhang W (2024) Suppression of nonlinear aeroelastic responses of graphene platelet-reinforced composite lattice sandwich plates using a nonlinear energy sink. Nonlinear Dyn 112:12925–12939

47. Yang SW, Hao YX, Zhang W, Ma WS, Wu MQ (2024) Nonlinear frequency and bifurcation of carbon fiber-reinforced polymer truncated laminated conical shell. J Vib Eng Technol 12(1):457–468

48. Yang SW, Wang ZQ, Hao YX, Zhang W, Liu LT, Ma WS, Kai G (2023) Static bending and stability analysis of sandwich conical shell structures with variable thickness core. Mech Adv Mater Struct. https://doi.org/10.1080/15376494.2023.2270545

49. Wang ZQ, Yang SW, Hao YX, Zhang W, Ma WS, Zhang XD (2023) Modeling and free vibration analysis of variable stiffness system for sandwich conical shell structures with variable thickness. Int J Struct Stab Dyn 23(15):2350171

50. Yang S, Hao Y, Zhang W, Liu L, Ma W (2022) Static and dynamic stability of carbon fiber reinforced polymer cylindrical shell subject to non-normal boundary condition with one generatrix clamped. Mathematics 10(9):1531

51. Yang SW, Wang ZQ, Hao YX, Zhang W, Ma WS, Niu Y (2024) Nonlinear dynamic response and bifurcation of variable thickness sandwich conical shell with internal resonance. Nonlinear Dyn 112:8931–8965

52. Chai S, Yang SW, Wang ZQ et al (2024) Variable stiffness and free vibration analysis of cylindrically curved plate with variable thickness graphene reinforced porous material. J Vib Eng Technol. https://doi.org/10.1007/s42417-024-01451-8

53. Grover N, Singh BN, Maiti DK (2013) New nonpolynomial shear-deformation theories for structural behavior of laminated-composite and sandwich plates. AIAA J 51(8):1861–1871